Bridging Experiment and Theory: Enhancing the Electrical Conductivities of Soft-Templated Niobium-doped Mesoporous Titania Films

Marvin Frisch*[a], Joachim Laun*[b], Julien Marquardt[c], Aleks Arinchtein[a], Katharina Bauerfeind[b], Denis Bernsmeier[a], Michael Bernicke[a], Thomas Bredow[b] and Ralph Kraehnert†[a]

[a]Department of Chemistry
Technical University of Berlin
Strasse des 17. Juni 124, D-10623 Berlin, Germany
†E-mail: ralph.kraehnert@tu-berlin.de

[b]Mulliken Center for Theoretical Chemistry, Institute of Physical and Theoretical Chemistry, University of Bonn
Beringstr. 4, D-53115 Bonn, Germany
E-mail: bredow@thch.uni-bonn.de

[c]Federal Institute for Materials Research and Testing (BAM)
Richard-Willstätter-Straße 11, D-12489 Berlin

Table of Contents

Experimental Section

Theoretical Calculations

For the presented DFT calculations, we applied two different approaches. On the one hand, relative phase stabilities were calculated using VASP[1–3]/900 eV/SCAN[4]. SCAN is a reasonable choice to calculate highly accurate thermodynamic and structural properties. On the other hand, meta-GGA functionals are not able to accurately describe the electronic structure, in particular the electronic band gap and the resulting electrical conductivity. For this reason, we have chosen a self-consistent hybrid approach with CRYSTAL17[5,6] based on the hybrid functional PW1PW[7] for the calculation of these properties, on the other hand. All computational details of both approaches are explicitly described in the following chapters.

To obtain the relative phase stability and the corresponding electronic sheet conductivity, $2{\times}2{\times}3$ rutile and $2{\times}3{\times}1$ anatase supercells were simulated. Each supercell was comprised of 24 stoichiometric units and Ti atoms were partially substituted by 1, 2, 4, 6, 8, 10 or 12 Nb atoms. All configurations show a maximum distribution of the substitute and are given in **SI-7&8**.

Relative phase stability

The density functional theory (DFT) calculations for the relative phase stabilities of rutile and anatase phase were performed with the Vienna *ab initio* program (VASP)[1–3] version 5.4.4 using the projector-augmented wave (PAW) approach of Joubert and Kresse.[8,9] The respective POTCAR files containing the PAW parameters were extracted from the VASP library. The PAWs with the largest valence-space available denoted as Ti_sv_GW (12 valence electrons (VE), $3s^23p^64s^24d^2$), Nb_sv_GW (13 VE, $3s^23p^64s^24d^3$) and O_GW (6 VE, $2s^23p^4$), which include the semi-core s and p shells, were applied. While keeping the symmetry, full structure relaxations were performed using the strongly constrained and appropriately normed (SCAN) functional[4], a k-spacing of 0.2 A^{-1} and a 900 eV energy cutoff to expand the Kohn-Sham

orbitals into plane wave basis sets. In the DFT calculations, most exchange-correlation functionals significantly over-stabilize the anatase phase compared to the rutile phase. Computationally expensive methods such as the random phase approximation (RPA)[10] or Diffusion Monte Carlo (DMC)[11] are able the predict the experimental phase stability[12] of rutile with respect to anatase of -2.61 ± 0.41 kJ mol^{-1} but are not feasible due to their prohibitive cost scaling. It is well-known that *meta*-GGA functionals such as SCAN systematically underestimate the electronic band gap for TiO_2 phases.[13] Nevertheless, SCAN is a reasonable choice to predict highly accurate thermodynamic and structural properties especially for semiconducting materials with reasonable computational effort.[14–16] The calculated relative phase stability of rutile vs. anatase of 3.56 kJ mol^{-1} per formula is in excellent agreement with the former DFT study of Sun *et al.*[13] showing values of 2.5 kJ mol^{-1} (SCAN), 9.1 kJ mol^{-1} (PBE) and 8.4 kJ mol^{-1} (HSE).

Sheet conductivity

To calculate the electrical sheet conductivities in dependency of Nb fraction in $Nb_xTi_{1-x}O_2$, DFT calculations were performed with the CRYSTAL17 program package version 1.0.2.[5,6] For global hybrid functional calculations the electronic band structure and the resulting electronic conductivity strongly depend on the system-independent Fock exchange fraction. Previous work[17–20] has shown that the dielectric-dependent self-consistent hybrid methods[21] provide high accuracy for electronic band gaps and absolute band positions. Therefore, we used the fully-automated algorithm[22] for the determination of the system-specific optimal Fock exchange for the PW1PW functional[7] as implemented in CRYSTAL17. The resulting Fock exchange is given as 15.1 % for the pure rutile, 18.0 % for the pure anatase phase and 0 % for all substituted phases. For undoped titania, this follows previous results[17] showing that the use of hybrid functionals is necessary for semiconducting oxides in order to obtain an accurate description of electronic band gaps. Since all substituted phases have a metallic ground state as

a consequence of n-type doping, the dielectric constant increases to large values during the self-consistent procedure and results in the pure PWGGA functional.

While keeping the respective symmetry, full structural relaxations were carried out using the self-consistent PW1PW functional, all-electron Gaussian-type basis sets for Ti and O[23], and ECP basis set[24] for Nb of triple-zeta with polarization quality. To reach SCF convergence for all conducting states we used a 8×8×8 Monkhorst-Pack grid and a denser 16×16×16 Gilat net for all optimizations. The truncation criteria for bi-electronic integrals were set to 10^{-7} for the overlap and penetration threshold for the Coulomb integrals and for the overlap threshold for HF exchange integrals. For the pseudo overlap in the HF exchange series, the truncation criteria were set to 10^{-14} and 10^{-42}. The SCF accuracy was set to 10^{-7} a. u. for optimizations of geometry. To estimate the electrical conductivity, we used the Boltzmann transport equation in relaxation time approximation as implemented as BOLTZTRA[6] in CRYSTAL17. We used a denser 12×12×12 Monkhorst-Pack grid, a 24×24×24 Gilat net and a relaxation time parameter of 10 fs to calculate the electrical conductivity at the Fermi level at 25 °C. The calculated conductivity is by definition a 3×3 tensor for a three-dimensional system, so we averaged the diagonal elements and discarded the small off-diagonal elements.

We have noticed that the calculated absolute conductivities are very sensitive to the density of the applied *k*-point grid. However, it was not possible to reach convergence due to computational effort. A reliable indicator to evaluate the electronic structure and the resulting conductivity is the fundamental band gap. With the applied method, the calculated fundamental band gaps of rutile (3.1 eV) and anatase (3.7 eV) are in good agreement with experimental results for rutile, 3.3-3.6 eV[25,26], and for anatase, 3.7-3.9 eV[27–29].

To gain a deeper insight in the electronic structure and the qualitative dependency of the electrical conductivity, we have additionally performed density of state (DOS) calculations as well as crystal orbital Hamiltonian population (COHP)[30] analyses, which provide a straightforward view into orbital- or atom-pair interactions such as bonding and antibonding

states and interaction strengths. These methods require a local description of the electronic structure in terms of atom-centered orbitals, which then allow the formation of the Hamiltonian matrix. For this reason, CRYSTAL17 is the perfect choice for COHP analyses, as it expands crystalline orbitals from atom-centered contracted Gaussian basis functions.[31] For the electrical conductivity, the bands near the Fermi level are of special interest, which are for the given substituted rutile phases primarily dominated by the metal d-orbitals or, more precisely, the $d_{x^2-y^2}$-orbitals showing a major contribution. Thus, we calculated the DOS and, additionally, the projected DOS (PDOS), as a Mulliken population weighted DOS, projected on the elements and all d-orbitals. For the COHP analyses, the interactions within the nearest neighbor atom-pairs Nb-Nb, Ti-Ti and Nb-Ti, as well as their corresponding $d_{x^2-y^2}$-orbitals, were computed, respectively. By convention, all COHP plots showing bonding (stabilizing) contributions show positive signs and antibonding (destabilizing) contributions show negative signs and are further denoted as -COHP. All PDOS and COHP calculations were performed in a range of ± 0.3 eV around the Fermi energy with identical settings as for the conductivity. The resulting plots are given in **SI-9**.

Raman Spectroscopy

In order to predict Raman spectra of bulk rutile and anatase phases, we performed vibrational frequency calculations (FREQCALC) using the CRYSTAL17 code with the PW1PW functional and the mentioned basis sets and truncation criteria. Hybrid DFT calculations have shown to predict highly accurate vibrational frequencies and corresponding Raman intensities for crystalline compounds.[32–35] For the calculated Raman intensities, the effects of the temperature at 25 °C and the wavelength of the incident beam of 633 nm were taken into account *via* RAMEXP. The calculated active Raman modes are illustrated as vertical bars in **Figure 2b** in the manuscript and the calculated values can be found in **SI-5** in the Supporting Information.

Experimental Details

Synthesis of soft-templated mesoporous $Nb_xTi_{1-x}O_2$ films

For the synthesis of mesoporous $Nb_xTi_{1-x}O_2$ films, niobium(V)chloride ($NbCl_5$, 99%) was purchased from *Alfa Aesar*, titanium(IV)chloride ($TiCl_4$, 99.9 %) and ethanol p. a. (EtOH, $\geq$ 99.8 %) were purchased from *VWR Chemicals*. Pluronic F-127 (PEO_{106}–PPO_{70}–PEO_{106}, M_w = 12 600 g mol^{-1}) was purchased from *Sigma-Aldrich*. All chemicals were used as received without any further purification. In a typical synthesis, 0.158 mL $TiCl_4$ were carefully dissolved in 2.50 mL EtOH (Ar) affording a clear solution (**I**). 0.451 g F-127 were dissolved in 3.00 mL EtOH (air) under stirring at 55 °C for 2 h (**II**). When a clear solution was obtained, 1.56 mL of (**II**) were added to 0.149 g $NbCl_5$ under stirring, affording a clear solution (**III**). After that, 1.79 mL of (**I**) were added to (**III**) and stirred for further 30 min at 55 °C in an oil bath (air). Dip-coating was performed in a controlled atmosphere in air (T = 25 °C, RH = 35 – 40 %) on various substrates. The films were dried for at least 10 min in the controlled atmosphere.

Substrate pre-treatment

$Nb_xTi_{1-x}O_2$ films were deposited on different substrates. Single-side polished Si-wafers were obtained from University Wafers showing a (100) orientation and cleaned with ethanol and heated in air for 2 h at 600 °C prior to film deposition. Si-wafers were used for SEM, TEM, GI-XRD and XPS. For the electrical conductivity measurements *via* impedance spectroscopy and Raman spectroscopy, SiO_2 substrates (Science Services GmbH) were used and cleaned using a mixture of KOH and *iso*propanol prior to film deposition.

Physicochemical characterization

SEM images were recorded at 10 kV on a JEOL 7401F. For EDX analysis, Quantax 400 from Bruker was used as spectroscopic device. EDX spectra were obtained at 20 kV. TEM images were taken using a FEI Tecnai G2 20 S-TWIN transmission electron microscope at 200 kV acceleration voltage on scraped off film-fragments deposited on carbon-coated copper grids. Images were evaluated with *ImageJ* freeware, version 1.48 (*www.imagej.nih.gov/ij/*). XRD

analysis was conducted using a Bruker D8 advance instrument using Cu-K$_\alpha$ radiation, grazing incidence mode and a Goebel mirror.

XPS measurements were performed with an AXIS Ultra DLD photoelectron spectrometer manufactured by Kratos Analytical (Manchester, UK). XPS spectra were recorded using monochromatic Al-K$_\alpha$ radiation for excitation, at a pressure of approximately $5 \cdot 10^{-9}$ mbar. The electron emission angle was 0° and the source-to-analyzer angle was 60°. The binding energy scale of the instrument was calibrated following a Kratos Analytical procedure using ISO15472 binding energy data. Spectra were taken by setting the instrument to the hybrid lens mode and the slot mode providing approximately a 300×700 μm² analysis area. Furthermore, the charge neutralizer was used. Survey spectra were recorded with a step size of 1 eV and a pass energy of 80 eV, high resolution spectra were recorded with a step size of 0.1 eV and a pass energy of 20 eV. Quantification was performed with Unifit 2021 using Scofield factor, the inelastic mean free pathway and the transmission function for the normalization of the peak area. For peak fitting a sum Gaussian-Lorentzian function was used. As background, a modified Tougaard background was used. Two independent areas for each $Nb_xTi_{1-x}O_2$ film on a polished silicon wafer as substrate were measured and an average value was calculated and reported in this work. Sheet conductivity measurements *via* impedance spectroscopy were performed using a 8×8 gold pin array as probe head with an altering polarity sequence. All measurements were conducted in the dark in a home-built setup to prevent any influence on electronic properties induced by the photoactivity of (doped) TiO_2 materials leading to the generation of excited charge carriers. A SP-200 potentiostat (Biologic) was used in a range between 100 mHz and 1 kHz. The obtained spectra (Nyquist impedance) were fitted using EIS Zfit software (EC-Lab version 11.33, Biologic). The Raman spectra were acquired by using a LabRam HR 800 instrument (Horiba Jobin Yvon) coupled to a BX41 microscope (Olympus). For both excitation and collection of the scattered light, a 100x/NA = 0.90 objective lens was employed. The system is equipped with a helium neon (HeNe) laser with a wavelength of 633 nm and 300 mm^{-1}

grating. The spectra were acquired with a liquid N_2-cooled (-126 °C operating temperature) charge-coupled device (CCD) camera (Symphony CCD, Horiba Jobin Yvon). Each spectrum was accumulated over six individual measurements, each with a measuring time of 20 seconds. In order to verify the homogeneity of the layers, at least five different positions were examined on each sample. The spectrometer entrance slit was 100 μm wide and the confocal pinhole was in the fully open position (1000 μm). Prior to the Raman experiment, the laser was allowed to stabilize for at least 2 h and the spectrometer was recalibrated against the most prominent mode of silicon at 520.7 cm^{-1}.

SI-1: Cross-section SEM images of mesoporous $Nb_xTi_{1-x}O_2$ films. Scale bar = 100 nm.

| 0 mol-% Nb	5 mol-% Nb	25 mol-% Nb	35 mol-% Nb	50 mol-% Nb
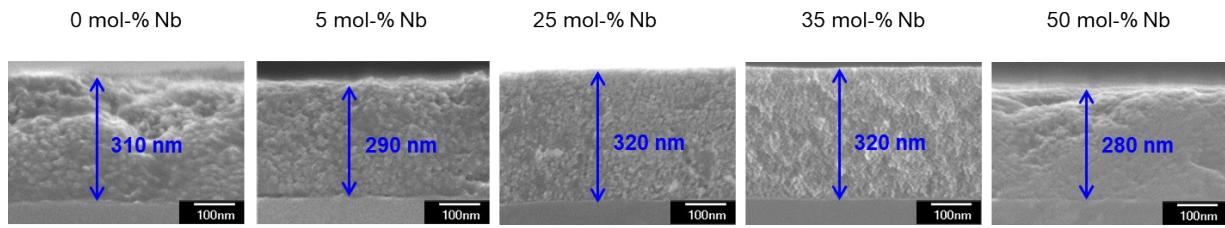
SI-2: EDX spectra of $Nb_xTi_{1-x}O_2$ films with templated mesoporosity on silicon substrates
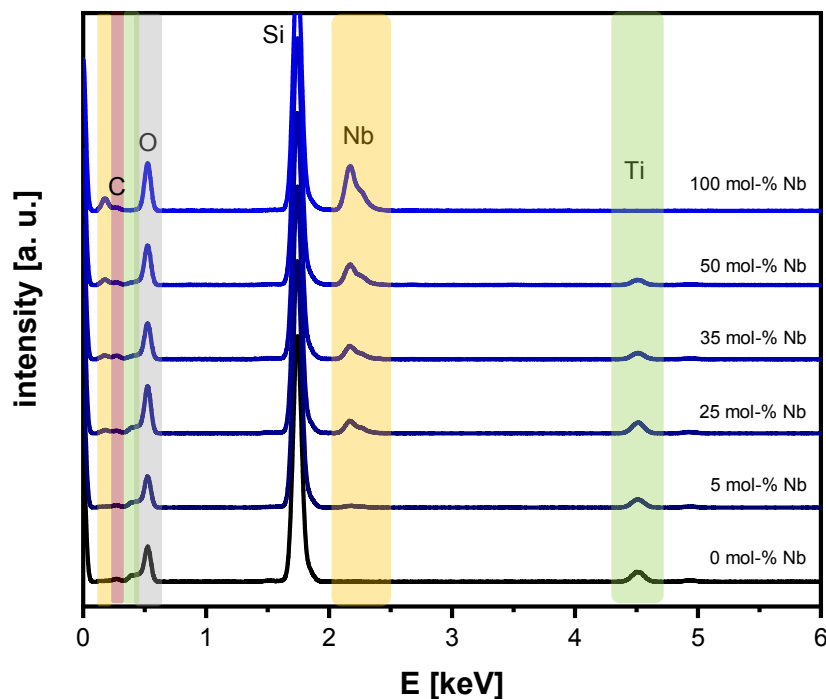
The obtained EDX spectra reveal the successful synthesis of templated mp. $Nb_xTi_{1-x}O_2$ films with varying molar Nb fraction. A quantification of the results from the spectra reveals only minor deviations between nominal and experimentally determined Nb fraction. At least three independent measurements on different areas of each film were performed and an average value for the Nb fraction was calculated and stated in the table below. As a reference, a mesoporous film containing 100 mol-% Nb was synthesized and investigated.

nominal Nb fraction [mol-%]	Nb fraction (EDX) [mol-%]
0.0	0.0
5.0	5.5
25.0	23.6
35.0	34.8
50.0	48.4
100.0	100.0

SI-3 Evaluation of XPS measurements of $Nb_xTi_{1-x}O_2$ films with templated mesoporosity on silicon substrates and discussion about the origin of the observed electrical conductivities in the context of literature reports
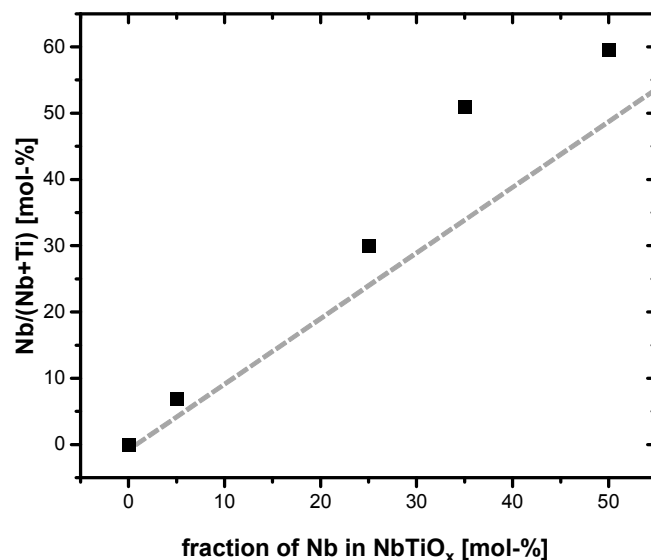
The parity plot of the relative fraction of Nb^{5+} species in mp. $Nb_xTi_{1-x}O_2$ indicates an increasing surface segregation for Nb fractions up to 35 mol-%. For 50 mol-% Nb, a less pronounced surface segregation becomes evident from surface analysis *via* XPS.
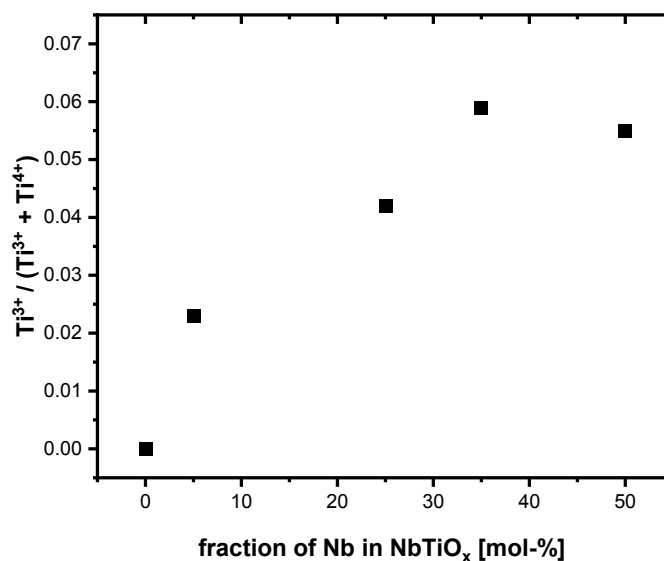
The XPS spectra of mp. $Nb_xTi_{1-x}O_2$ films show an increase in relative Ti^{3+} fraction with increasing incorporation of Nb atoms. The substitution of titanium with niobium atoms in the

13

lattice of the doped oxides induces charge imbalance. Hence, Ti^{3+} species are formed to counterbalance the Nb^{5+} species in the substituted lattice. For 35 mol-% Nb in $Nb_xTi_{1-x}O_2$, the relative amount of reduced Ti^{3+} species appears particularly high. In literature[36,37], two different charge compensation mechanisms by the substitutional incorporation of Nb^{5+} into the titania lattice (primarily Ti^{4+} species) are discussed. In the first, for every Nb^{5+} incorporated into the lattice, one Ti^{4+} is reduced to one Ti^{3+}. In the second, per four Nb^{5+} one Ti vacancy is formed.[38] Based on their XPS data on mp. $Nb_xTi_{1-x}O_2$ films, Yue *et al.*[36] reported that for lower fractions of Nb^{5+}, *i. e.* lower fractions of Nb in $Nb_xTi_{1-x}O_2$, charge compensation occurs *via* generation of Ti vacancies, whereas, for higher fractions of Nb^{5+}, free electrons lead to a higher electrical conductivity. In this context, however, it has to be mentioned that in their study, Yue *et al.* found the maximum in electrical conductivity for only 5 mol-% Nb in $Nb_xTi_{1-x}O_2$. For 10 mol-% Nb, the authors reported declined electrical conductivities, as a result of electron trapping at Ti^{4+} sites and, thus, reduced ionization efficiencies. Furthermore, the herein examined phase transition from anatase toward rutile phase was not observed at all in their previous study.

SI-4: GI-XRD pattern for synthesized mp. $Nb_xTi_{1-x}O_2$ films with Nb fraction > 35 mol-%
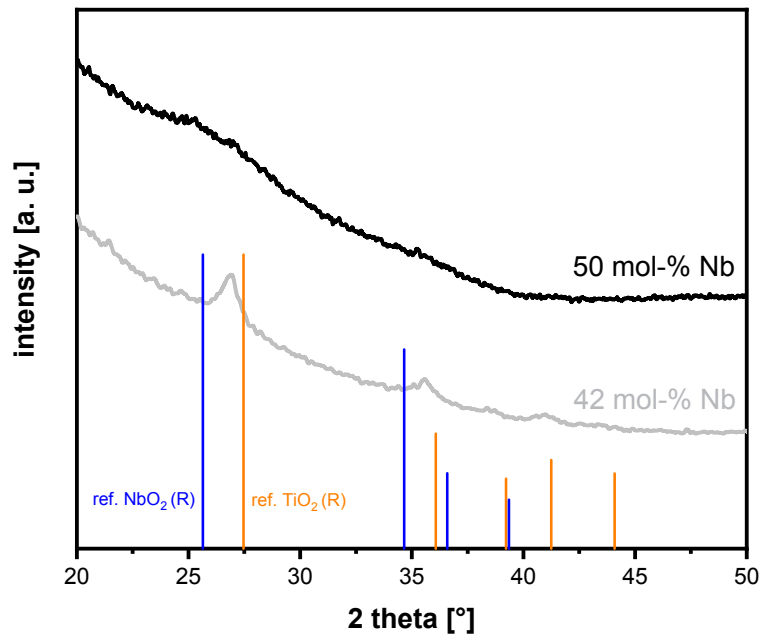
For Nb fractions of 42 mol-% Nb, distinct shifts of the reflections to lower 2 theta values can be observed compared to bare rutile TiO_2. According to the GI-XRD measurements shown in the above figure, the reflections are shifted to values between those of rutile TiO_2 (orange pattern) and rutile NbO_2 (blue pattern). This leads to the conclusion that a nanocrystalline material was obtained, in which Nb ions partially substitute Ti ions in the lattice with predominantly rutile phase. For an increasing fraction of Nb, *i. e.* for 50 mol-% Nb, a significant decrease in crystallinity can be deduced from the diffraction pattern. Accordingly, it seems more appropriate to describe this X-ray amorphous system as a solid solution, rather than a doped titanium oxide.

SI-5: Calculated rutile and anatase Raman active modes with the given symmetry indicated by the Mulliken notation. All intensities are stated relative to the highest intensity in arbitrary units.

rutile				
symmetry	B_{1g}	E_g	A_{1g}	B_{2g}
frequency [cm $^{-1}$]	140	460	611	830
intensity [a. u.]	7.2	742.3	1000.0	0

anatase					
symmetry	E_g	B_{1g}	A_{1g}	B_{1g}	E_g
frequency [cm $^{-1}$]	137	399	519	520	641
intensity [a. u.]	1000.0	98.9	18.6	82.7	197.0

SI-6: Calculated relative electrical conductivities σ in dependency of molar Nb fraction in $Nb_xTi_{1-x}O_2$. Values for σ are given in $S\ cm^{-1}$.

fraction of Nb [mol-%]	calc. σ_{rutile} [S cm^{-1}]	calc. $\sigma_{anatase}$ [S cm^{-1}]
0.0	4.22E-08	6.40E-07
4.2	1.58E-06	1.69E-06
8.3	2.42E-06	2.18E-06
16.7	4.55E-06	2.80E-06
25.0	4.50E-06	1.96E-06
33.3	8.04E-06	2.35E-06
41.7	5.03E-06	2.01E-06
50.0	5.84E-06	1.18E-06

SI-7: Fractional coordinates of the rutile 2×2×3 and the anatase 2×3×1 supercells.

The lattice parameters are given as a = 4.587 Å and c = 2.954 Å in $P4_2/mnm$ for rutile[39] and as a' = 3.782 Å and c' = 9.502 Å in $I4_1/amd$ for anatase[39].

#	atom	rutile			anatase		
		x/a	y/b	z/c	x/a'	y/b'	z/c'
1	Ti	0.0000	0.0000	0.0000	0.0000	-0.1667	0.2500
2	Ti	0.0000	0.0000	0.3333	0.2500	0.0000	-0.2500
3	Ti	0.0000	0.0000	-0.3333	-0.5000	0.1667	0.2500
4	Ti	0.0000	-0.5000	0.0000	-0.2500	0.3333	-0.2500
5	Ti	0.0000	-0.5000	0.3333	0.0000	-0.5000	0.2500
6	Ti	0.0000	-0.5000	-0.3333	0.2500	-0.3333	-0.2500
7	Ti	-0.5000	0.0000	0.0000	-0.5000	-0.1667	0.2500
8	Ti	-0.5000	0.0000	0.3333	-0.2500	0.0000	-0.2500
9	Ti	-0.5000	0.0000	-0.3333	0.0000	0.1667	0.2500
10	Ti	-0.5000	-0.5000	0.0000	0.2500	0.3333	-0.2500
11	Ti	-0.5000	-0.5000	0.3333	-0.5000	-0.5000	0.2500
12	Ti	-0.5000	-0.5000	-0.3333	-0.2500	-0.3333	-0.2500
13	Ti	-0.2500	-0.2500	-0.1667	0.0000	0.0000	-0.5000
14	Ti	-0.2500	-0.2500	0.1667	0.2500	0.1667	0.0000
15	Ti	-0.2500	-0.2500	-0.5000	-0.5000	0.3333	-0.5000
16	Ti	-0.2500	0.2500	-0.1667	-0.2500	-0.5000	0.0000
17	Ti	-0.2500	0.2500	0.1667	0.0000	-0.3333	-0.5000
18	Ti	-0.2500	0.2500	-0.5000	0.2500	-0.1667	0.0000
19	Ti	0.2500	-0.2500	-0.1667	-0.5000	0.0000	-0.5000
20	Ti	0.2500	-0.2500	0.1667	-0.2500	0.1667	0.0000
21	Ti	0.2500	-0.2500	-0.5000	0.0000	0.3333	-0.5000
22	Ti	0.2500	0.2500	-0.1667	0.2500	-0.5000	0.0000
23	Ti	0.2500	0.2500	0.1667	-0.5000	-0.3333	-0.5000
24	Ti	0.2500	0.2500	-0.5000	-0.2500	-0.1667	0.0000
25	O	0.1521	0.1521	0.0000	0.2500	0.0000	-0.4582
26	O	0.1521	0.1521	0.3333	-0.5000	0.1667	0.0418
27	O	0.1521	0.1521	-0.3333	-0.2500	0.3333	-0.4582
28	O	0.1521	-0.3480	0.0000	0.0000	-0.5000	0.0418
29	O	0.1521	-0.3480	0.3333	0.2500	-0.3333	-0.4582
30	O	0.1521	-0.3480	-0.3333	-0.5000	-0.1667	0.0418
31	O	-0.3480	0.1521	0.0000	-0.2500	0.0000	-0.4582
32	O	-0.3480	0.1521	0.3333	0.0000	0.1667	0.0418
33	O	-0.3480	0.1521	-0.3333	0.2500	0.3333	-0.4582
34	O	-0.3480	-0.3480	0.0000	-0.5000	-0.5000	0.0418
35	O	-0.3480	-0.3480	0.3333	-0.2500	-0.3333	-0.4582
36	O	-0.3480	-0.3480	-0.3333	0.0000	-0.1667	0.0418
37	O	-0.1521	-0.1521	0.0000	0.2500	-0.1667	0.2082
38	O	-0.1521	-0.1521	0.3333	-0.5000	0.0000	-0.2918
39	O	-0.1521	-0.1521	-0.3333	-0.2500	0.1667	0.2082
40	O	-0.1521	0.3480	0.0000	0.0000	0.3333	-0.2918
41	O	-0.1521	0.3480	0.3333	0.2500	-0.5000	0.2082
42	O	-0.1521	0.3480	-0.3333	-0.5000	-0.3333	-0.2918

|							
43	O	0.3480	-0.1521	0.0000	-0.2500	-0.1667	0.2082
44	O	0.3480	-0.1521	0.3333	0.0000	0.0000	-0.2918
45	O	0.3480	-0.1521	-0.3333	0.2500	0.1667	0.2082
46	O	0.3480	0.3480	0.0000	-0.5000	0.3333	-0.2918
47	O	0.3480	0.3480	0.3333	-0.2500	-0.5000	0.2082
48	O	0.3480	0.3480	-0.3333	0.0000	-0.3333	-0.2918
49	O	-0.0980	0.0980	-0.1667	0.0000	-0.1667	0.4582
50	O	-0.0980	0.0980	0.1667	0.2500	0.0000	-0.0418
51	O	-0.0980	0.0980	-0.5000	-0.5000	0.1667	0.4582
52	O	-0.0980	-0.4021	-0.1667	-0.2500	0.3333	-0.0418
53	O	-0.0980	-0.4021	0.1667	0.0000	-0.5000	0.4582
54	O	-0.0980	-0.4021	-0.5000	0.2500	-0.3333	-0.0418
55	O	0.4021	0.0980	-0.1667	-0.5000	-0.1667	0.4582
56	O	0.4021	0.0980	0.1667	-0.2500	0.0000	-0.0418
57	O	0.4021	0.0980	-0.5000	0.0000	0.1667	0.4582
58	O	0.4021	-0.4021	-0.1667	0.2500	0.3333	-0.0418
59	O	0.4021	-0.4021	0.1667	-0.5000	-0.5000	0.4582
60	O	0.4021	-0.4021	-0.5000	-0.2500	-0.3333	-0.0418
61	O	0.0980	-0.0980	-0.1667	0.0000	0.0000	0.2918
62	O	0.0980	-0.0980	0.1667	0.2500	0.1667	-0.2082
63	O	0.0980	-0.0980	-0.5000	-0.5000	0.3333	0.2918
64	O	0.0980	0.4021	-0.1667	-0.2500	-0.5000	-0.2082
65	O	0.0980	0.4021	0.1667	0.0000	-0.3333	0.2918
66	O	0.0980	0.4021	-0.5000	0.2500	-0.1667	-0.2082
67	O	-0.4021	-0.0980	-0.1667	-0.5000	0.0000	0.2918
68	O	-0.4021	-0.0980	0.1667	-0.2500	0.1667	-0.2082
69	O	-0.4021	-0.0980	-0.5000	0.0000	0.3333	0.2918
70	O	-0.4021	0.4021	-0.1667	0.2500	-0.5000	-0.2082
71	O	-0.4021	0.4021	0.1667	-0.5000	-0.3333	0.2918
72	O	-0.4021	0.4021	-0.5000	-0.2500	-0.1667	-0.2082

SI-8: Configurations of Nb-substituted rutile and anatase supercells. The indices of the substituted atoms refer to the labeling in **SI-7**.

fraction of Nb [mol-%]	number of Nb atoms	index$_{rutile}$	index$_{anatase}$
4.2	**1**	15	1
8.3	**2**	15,22	1,15
16.7	**4**	15,16,19,24	1,8,15,16
25.0	**6**	8,11,15,18,19,22	1,2,3,15,20,22
33.3	**8**	3,6,9,12,14,17,20,23	2,7,9,12,15,17,20,22
41.7	**10**	1,4,8,9,11,13,16,18,20,23	1,2,7,9,12,15,17,19,20,22
50.0	**12**	1,4,8,9,11,12,13,15,16,18,20,23	1,2,3,7,9,12,15,17,19,20,22,24

SI-9: Projected density of states (PDOS) (a), crystal orbital Hamiltonian population (-COHP) of the nearest neighbor atom (b) and orbital (c) interactions for all substituted rutile supercells. PDOS are given in states per eV, and -COHP are given per eV. By convention, all -COHP plots showing bonding (stabilizing) contributions are positive and antibonding (destabilizing) contributions are negative in sign. All energies are shown relative to the Fermi level $\varepsilon_F = 0$.
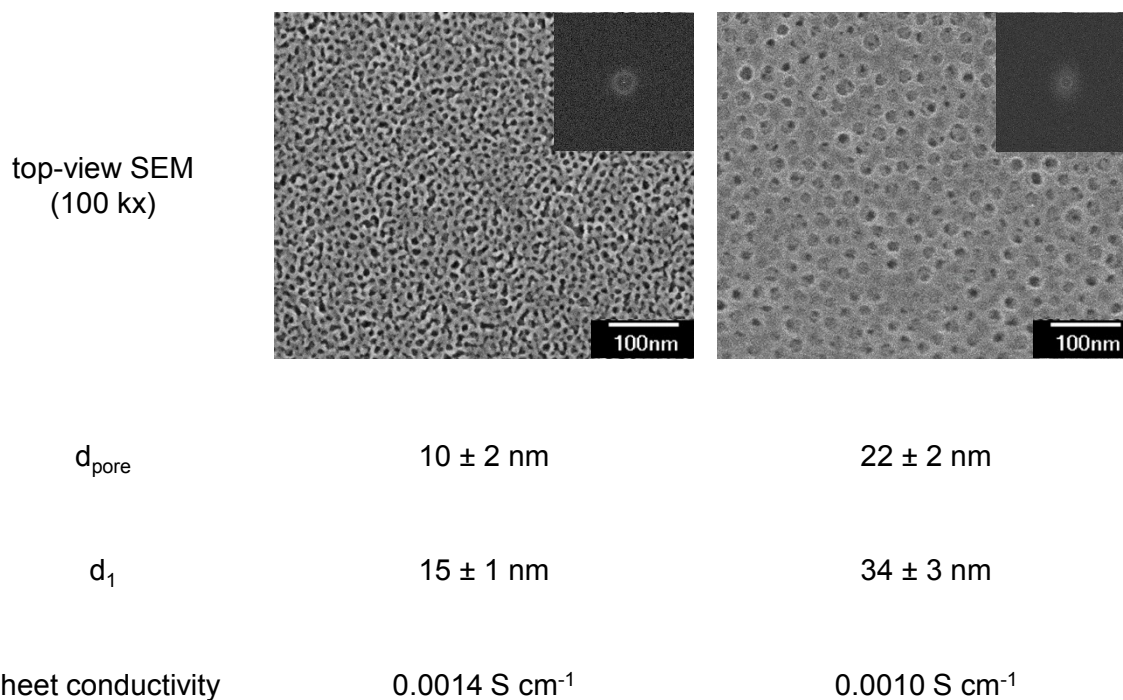
(b)

(c)
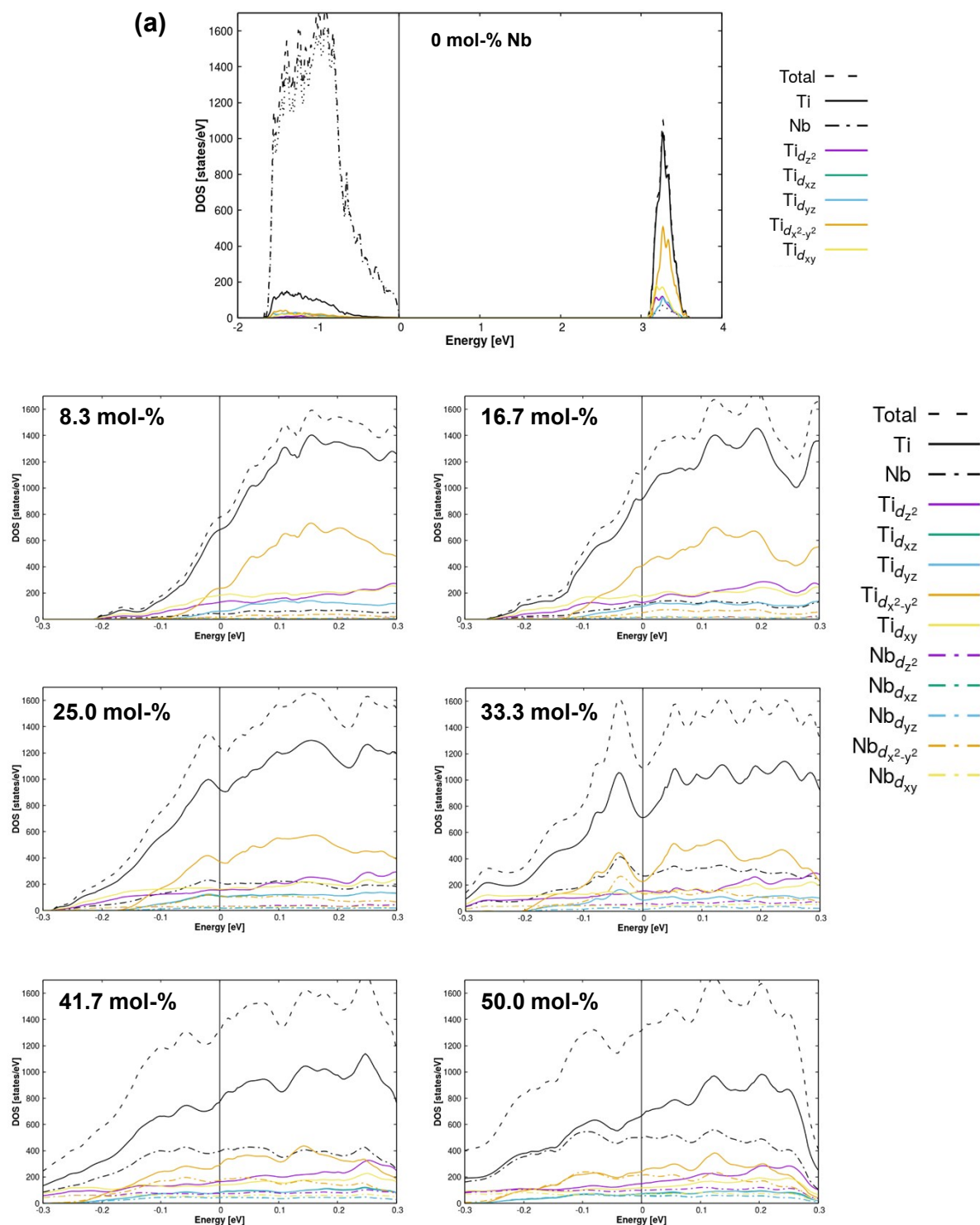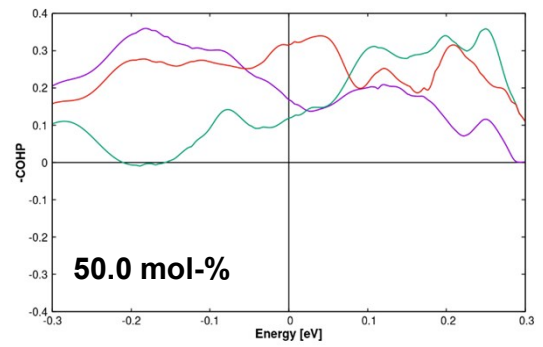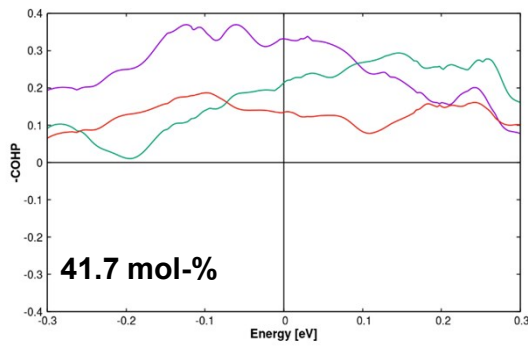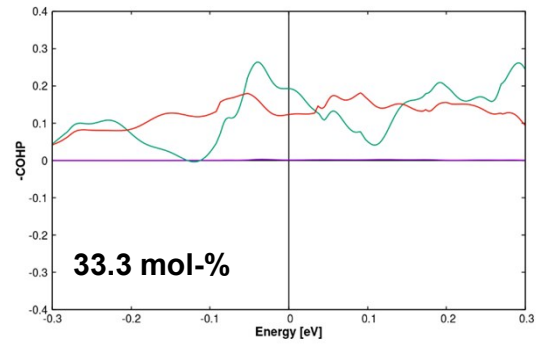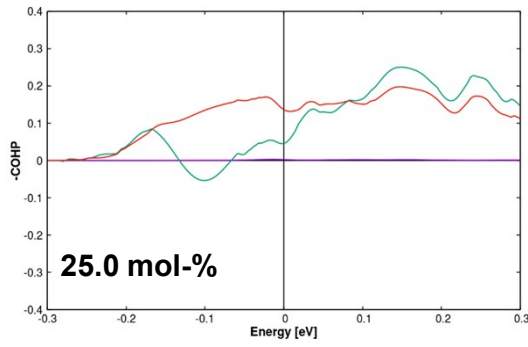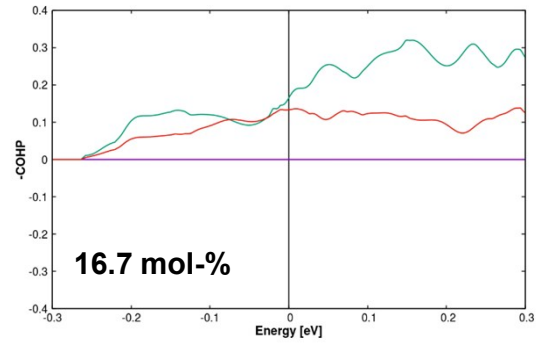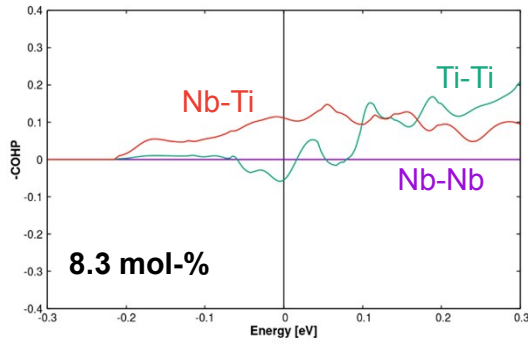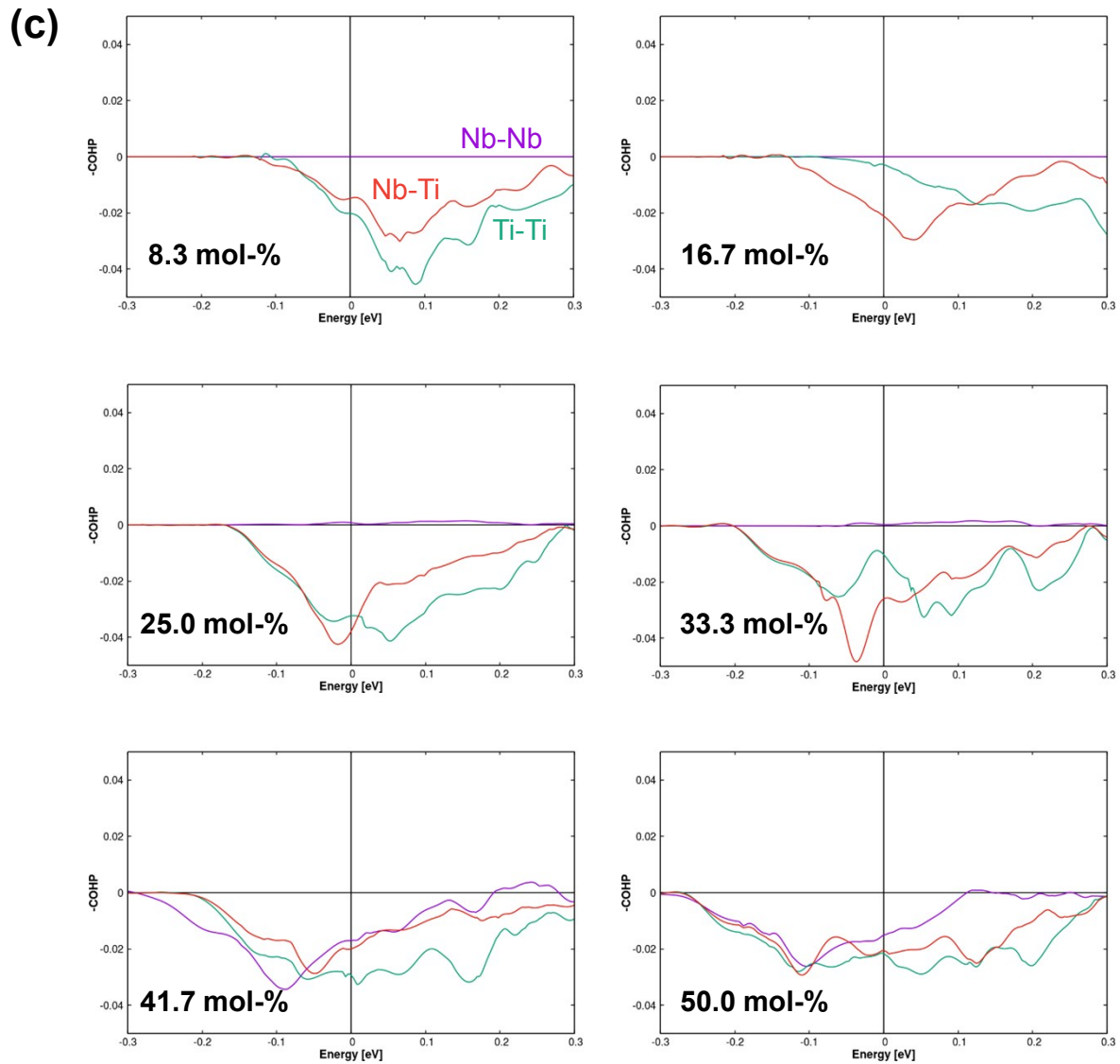
The general observed trend of the calculated electrical conductivity in dependency of molar Nb fraction is discussed by the PDOS and -COHP analyses for the substituted rutile supercells. Increasing the Nb fraction up to 25 mol-% leads to a systematic increase of the states at the Fermi level. This behavior seems reasonable due to the fact that n-type doping increases the electron density and, thus, shifts the Fermi level to higher energies.

Mulliken population analyses confirm this trend, as the occupation of Ti 3d-orbitals, in particular 3d_{z^2}, 3d_{x2-y2} and 3d_{xy}, increases with increasing Nb content. This is of particular importance, as these orbitals dominate the states around the Fermi level and significantly

contribute to the conductivity of the substituted phases. We do not observe a localization of charge density on particular Ti atoms, not even for small Nb fractions. This can be due to the application of a GGA method which, in general, tends to delocalize electron density.

For 33 mol-% Nb, the number of states at the Fermi level is lower than for smaller dopant fractions. Yet, there is a larger amount of states just below the Fermi level. Up to 33 mol-% of Nb, no Nb-Nb interactions occur, while bonding Nb-Ti interactions systematically increase and thus explain the rise in electrical conductivity. For 41.7 and 50.0 mol-% Nb, strong stabilizing Nb-Nb interactions appear resulting in decreasing conductivities due to more localized electrons. Overall, the maximum conductivity can be explained by a combination of increasing electron density while avoiding Nb-Nb interactions.

SI-10: Investigations on the impact of mesoporosity on the observed electrical properties for films synthesized with different polymer templates with 35 mol-% Nb in $Nb_xTi_{1-x}O_2$ as an illustrative example.

top-view SEM (100 kx)		
d_{pore}	10 ± 2 nm	22 ± 2 nm
d_1	15 ± 1 nm	34 ± 3 nm
sheet conductivity	0.0014 S cm^{-1}	0.0010 S cm^{-1}

Due to the fact that all herein presented theoretical models and calculations do not consider any (meso-)porosity, as this lies beyond the scope of our study, additional experiments were performed. As illustrative example, a different tri-block copolymer template was used in the synthesis of 35 mol-% Nb in $Nb_xTi_{1-x}O_2$ and compared to the F-127 templated film with the same dopant fraction.

As illustrated in the figure above, the films synthesized using PEO_{213}-PB_{184}-PEO_{213} as structure-directing agent (right) show larger pore sizes and thicker pore walls compared to the F-127-templated films (left). A larger average inter-pore distance for the PEO_{213}-PB_{184}-PEO_{213}-templated films can be confirmed by comparing the respective FFT (insets in both SEM images). Accordingly, PEO_{213}-PB_{184}-PEO_{213} forms larger spherical micelles and, hence, leads to larger pores and inter-pore distances after calcination. For both films, similar electrical sheet conductivities were found in experiment.

In general, our experimental results coincide well with the calculated data providing bulk properties, as surface effects seem to play only a minor role. One of the main advantages of our synthesis method for niobium-doped titania *via* dip-coating and the addition of a structure-directing agent is the high homogeneity of the resulting materials. Comparable wall- and sheet-thicknesses of the synthesized films enable a systematic study of their electronic properties in dependency of a single parameter which can be precisely adjusted, for example, the dopant fraction. The experimentally observed high crystallinity of the solids, the independence of the pore size and the interface with insulating air inside the pores confirm the dominance of the bulk properties in our systems.

References

[1]   G. Kresse, J. Hafner, *Phys. Rev. B* **1993**, *47*, 558–561.

[2]   G. Kresse, J. Furthmüller, *Comput. Mater. Sci.* **1996**, *6*, 15–50.

[3]   G. Kresse, J. Furthmüller, *Phys. Rev. B* **1996**, *54*, 11169–11186.

[4]   J. Sun, A. Ruzsinszky, J. P. Perdew, *Phys. Rev. Lett.* **2015**, *115*, 036402.

[5]   R. Dovesi, A. Erba, R. Orlando, C. M. Zicovich-Wilson, B. Civalleri, L. Maschio, M. Rérat, S. Casassa, J. Baima, S. Salustro, B. Kirtman, *Wiley Interdiscip. Rev. Comput. Mol. Sci.* **2018**, *8*, 1360.

[6]   S. C. R. Dovesi, V. R. Saunders, C. Roetti, R. Orlando, C. M. Zicovich-Wilson, F. Pascale, B. Civalleri, K. Doll, N. M. Harrison, I. J. Bush, P. D'Arco, M. Llunell, M. Causà, Y. Noël, L. Maschio, A. Erba, M. Rerat, *CRYSTAL17 User's Manual*, University of Torino, **2017**.

[7]   T. Bredow, A. R. Gerson, *Phys. Rev. B* **2000**, *61*, 5194–5201.

[8]   P. E. Blöchl, *Phys. Rev. B* **1994**, *50*, 17953–17979.

[9]   G. Kresse, D. Joubert, *Phys. Rev. B* **1999**, *59*, 1758–1775.

[10]   Z.-H. Cui, F. Wu, H. Jiang, *Phys. Chem. Chem. Phys.* **2016**, *18*, 29914–29922.

[11]   Y. Luo, A. Benali, L. Shulenburger, J. T. Krogel, O. Heinonen, P. R. C. Kent, *New J. Phys.* **2016**, *18*, 113049.

[12]   M. R. Ranade, A. Navrotsky, H. Z. Zhang, J. F. Banfield, S. H. Elder, A. Zaban, P. H. Borse, S. K. Kulkarni, G. S. Doran, H. J. Whitfield, *Proc. Natl. Acad. Sci.* **2002**, *99*, 6476–6481.

[13]   Y. Zhang, J. W. Furness, B. Xiao, J. Sun, *J. Chem. Phys.* **2019**, *150*, 014105.

[14]   Y. Hinuma, H. Hayashi, Y. Kumagai, I. Tanaka, F. Oba, *Phys. Rev. B* **2017**, *96*, 094102.

[15]   Y. Zhang, D. A. Kitchaev, J. Yang, T. Chen, S. T. Dacek, R. A. Sarmiento-Pérez, M. A. L. Marques, H. Peng, G. Ceder, J. P. Perdew, J. Sun, *npj Comput. Mater.* **2018**, *4*, 9.

[16]   C. Shahi, J. Sun, J. P. Perdew, *Phys. Rev. B* **2018**, *97*, 094111.

[17]   J. He, C. Franchini, *J. Phys. Condens. Matter* **2017**, *29*, 454004.

[18]   D. Fritsch, B. J. Morgan, A. Walsh, *Nanoscale Res. Lett.* **2017**, *12*, 19.

[19]   Y. Hinuma, Y. Kumagai, I. Tanaka, F. Oba, *Phys. Rev. B* **2017**, *95*, 075302.

[20]   M. Hochheim, T. Bredow, *Phys. Rev. B* **2018**, *97*, 235447.

[21]   J. H. Skone, M. Govoni, G. Galli, *Phys. Rev. B* **2014**, *89*, 195112.

[22]   A. Erba, *J. Phys. Condens. Matter* **2017**, *29*, 314001.

[23]   D. Vilela Oliveira, J. Laun, M. F. Peintinger, T. Bredow, *J. Comput. Chem.* **2019**, *40*, 2364–2376.

[24]   J. Laun, D. Vilela Oliveira, T. Bredow, *J. Comput. Chem.* **2018**, *39*, 1285–1290.

[25]   Y. Tezuka, S. Shin, T. Ishii, T. Ejima, S. Suzuki, S. Sato, *J. Phys. Soc. Japan* **1994**, *63*, 347–357.

[26]   S. Rangan, S. Katalinic, R. Thorpe, R. A. Bartynski, J. Rochford, E. Galoppini, *J. Phys. Chem. C* **2010**, *114*, 1139–1147.

[27]   Z. Wang, U. Helmersson, P.-O. Käll, *Thin Solid Films* **2002**, *405*, 50–54.

[28]   B. Liu, L. Wen, X. Zhao, *Mater. Chem. Phys.* **2007**, *106*, 350–353.

[29]   M. M. Hasan, A. S. M. A. Haseeb, R. Saidur, H. H. Masjuki, M. Hamdi, *Opt. Mater. (Amst).* **2010**, *32*, 690–695.

[30]   R. Dronskowski, P. E. Bloechl, *J. Phys. Chem.* **1993**, *97*, 8617–8624.

[31]   M. T. Ruggiero, A. Erba, R. Orlando, T. M. Korter, *Phys. Chem. Chem. Phys.* **2015**, *17*, 31023–31029.

[32]   L. Valenzano, F. J. Torres, K. Doll, F. Pascale, C. M. Zicovich-Wilson, R. Dovesi, *Zeitschrift für Phys. Chemie* **2006**, *220*, 893–912.

[33]   F. Pascale, C. M. Zicovich-Wilson, F. López Gejo, B. Civalleri, R. Orlando, R. Dovesi, *J. Comput. Chem.* **2004**, *25*, 888–897.

[34]   F. Pascale, C. M. Zicovich-Wilson, R. Orlando, C. Roetti, P. Ugliengo, R. Dovesi, *J.*

Phys. Chem. B **2005**, *109*, 6146–6152.

[35] B. Montanari, B. Civalleri, C. M. Zicovich-Wilson, R. Dovesi, *Int. J. Quantum Chem.* **2006**, *106*, 1703–1714.

[36] J. Yue, C. Suchomski, P. Voepel, R. Ellinghaus, M. Rohnke, T. Leichtweiss, M. T. Elm, B. M. Smarsly, *J. Mater. Chem. A* **2017**, *5*, 1978–1988.

[37] L. De Trizio, R. Buonsanti, A. M. Schimpf, A. Llordes, D. R. Gamelin, R. Simonutti, D. J. Milliron, *Chem. Mater.* **2013**, *25*, 3383–3390.

[38] X. Lü, X. Mou, J. Wu, D. Zhang, L. Zhang, F. Huang, F. Xu, S. Huang, *Adv. Funct. Mater.* **2010**, *20*, 509–515.

[39] J. K. Burdett, T. Hughbanks, G. J. Miller, J. W. Richardson, J. V. Smith, *J. Am. Chem. Soc.* **1987**, *109*, 3639–3646.